Long-lived Topological Flatband Excitons in Semiconductor Moiré Heterostructures: a Bosonic Kane-Mele Model Platform

Ming Xie,[1,*] Mohammad Hafezi,[2] and Sankar Das Sarma[1,2]

[1] *Condensed Matter Theory Center, Department of Physics, University of Maryland, College Park, Maryland 20742, USA*
[2] *Joint Quantum Institute, Department of Physics, University of Maryland, College Park, Maryland 20742, USA*

(Dated: March 4, 2024)

Moiré superlattices based on two-dimensional transition metal dichalcogenides (TMDs) have emerged as a highly versatile and fruitful platform for exploring correlated topological electronic phases. One of the most remarkable examples is the recently discovered fractional quantum anomalous Hall effect (FQAHE) under zero magnetic field. Here we propose a minimal structure that hosts long-lived excitons—a ubiquitous bosonic excitation in TMD semiconductors—with narrow topological bosonic bands. The nontrivial exciton topology originates from hybridization of moiré interlayer excitons, and is tunable by controlling twist angle and electric field. At small twist angle, the lowest exciton bands are isolated from higher energy bands, and provides a solid-state realization of bosonic Kane-Mele model with topological flatbands, which could potentially support the bosonic version of FQAHE.

Introduction.—Owing to their narrow bandwidths and intertwined electronic wavefunctions, moiré superlattices formed from overlaying two-dimensional TMD semiconductors have become a unique crossroad where strong electron correlations and nontrivial topology meet, under unprecedented controllability in both directions. In TMD superlattices where band topology is trivial, a plethora of strongly correlated phenomena, such as Mott insulators, generalized Wigner crystals, and metal-insulator transitions, have been identified [1–12]. Recently, in TMD superlattices featuring topological bands, experimental studies observed correlated phases with non-trivial topological characteristics [13–21], including both integer and fractional quantum anomalous Hall states. The latter, also referred to as fractional Chern insulators, is observed for the first time in experiments after being proposed for over a decade [22–26]. These observations establish TMD moiré superlattices as promising candidates for solid-state fermionic quantum simulations.

The drastic influence of the long-period moiré pattern extends to excitons—tightly-bound electron-hole pair excitations—in TMD moiré superlattices, rendering their localization on moiré lattices [27–38]. Remarkably, recent experiments discovered a correlated incompressible state of excitons [39–42], or a bosonic Mott insulator, in TMD moiré heterobilayers, breaking new grounds for exploring many-body systems of bosons. The moiré modulation in these superlattices leads to localized excitons seating on a triangular lattice and with strong on-site interactions, effectively simulating the Bose-Hubbard model. The emergence of localized bosonic lattices can be understood as the formation of trivial excitonic moiré bands with narrow bandwidths. One intriguing question arises: Is it possible to form topological moiré bands for excitons, thereby paving the way to achieve bosonic correlated topological phases, such as bosonic fractional Chern insulators?

It was understood that excitons in the $+K$ and $-K$ valleys of TMD monolayers have non-zero berry curvatures due to valley-momentum coupling induced by electron-hole exchange interactions [44–47]. Based on this, F. Wu and coworkers [34] showed that when such intralayer exciton is subjected to a periodic moiré potential, the resulting low-energy moiré exciton bands can have a definite Chern number, provided an effective Zeeman field for the exciton pseudospin is included. However, one critical issue that remains unaddressed in this scenario is the short lifetime of excitons, which is detrimental for experimental realization of many-body states of excitons. Intralayer excitons are known to have large optical dipole moment responsible for their short recombination lifetime; they decay rapidly before a quasi-equilibrium population of excitons can be established. The fact that the strength of the valley-momentum coupling is proportional to the optical dipole moment places topology and long lifetime at odds with each other.

In this Letter, we propose a minimal TMD moiré heterostructure capable of supporting excitons that are both long-lived and topological. It is based on interlayer moiré excitons whose optical dipole moments nearly vanish due to layer separation of their constituent electron and hole. The topology of the exciton moiré bands originates from spatially varying hybridization of interlayer excitons situated in different layers of the moiré heterostructure. This mechanism does not involve the exchange-induced exciton berry curvature, thereby avoiding the conflict between topology and long lifetime. We develop an effective bosonic continuum model for the interlayer moiré excitons. The valley-projected exciton bandstructure features a rich set of bosonic topological bands with opposite Chern numbers for opposite valley pseudo-spins. We find that, as the twist angle is varied, the band-

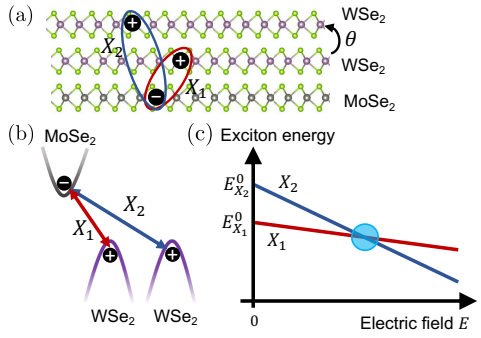

FIG. 1. (a) Schematic illustration of the proposed moiré heterostructure. The WSe_2 layers are twisted relative to each other by an angle θ while the $MoSe_2$ layer is rotation aligned with its neighboring WSe_2 layer. (b) The corresponding band diagram hosting the two low-energy interlayer excitons, X_1 and X_2, illustrated in (a). (c) Energy of the X_1 and X_2 excitons as a function of vertical electric field.

width of the lowest exciton band exhibits a minimum at a "magic" angle. At small twist angles, the pair of isolated lowest-energy exciton bands provides a first solid-state realization of the bosonic Kane-Mele model with nearly-flat topological bands.

Moiré heterostructure.—The proposed structure consists of a twisted WSe_2 ($tWSe_2$) homobilayer stacked on top of a $MoSe_2$ monolayer, with rotation alignment between the interfacing WSe_2 and $MoSe_2$ layers, as illustrated in Fig. 1(a). We have chosen TMD layers with a common chalcogen element (i.e., selenium), for their negligible mismatch in lattice constant, to avoid unimportant complications due to the formation of a second moiré pattern at the hetero-interface. In this regard, our theory applies to the general $tMX_2/M'X_2$ moiré heterostructure, where M, M′ represent different transition metal atoms, W or Mo, and X represents a S, Se or Te atom [43]. It will becomes clear below that the twisted WX_2 part provides the moiré modulated hybridization critical in our theory.

The $tWSe_2/MoSe_2$ heterostructure feature a type-II band alignment with a momentum-direct interlayer bandgap between the conduction band in the $MoSe_2$ and the valence band in the $tWSe_2$ at the $\pm K$ valleys [Fig. 1(b)]. The lowest energy excitons are the intravalley interlayer excitons formed by electrons in the $MoSe_2$ layer and holes in the middle and top WSe_2 layers, labeled as X_1 and X_2, respectively. Because of their different electron-hole vertical separations, X_1 and X_2 excitons have different binding energies. Their relative energies can be tuned by a perpendicular electric field E [Fig. 1(c)]. Assuming both interlayer spacings between neighboring layers are d, the exciton energy is given by $E_{X_l} = E^0_{X_l} - eEld$ (with $e > 0$), where $l = 1, 2$ and $E^0_{X_l}$ is the exciton energy at $E = 0$. As we demonstrate below, interesting physics occurs when X_1 and X_2 are close in energy and hybridize significantly with each other (highlighted by the cyan circle in Fig. 1(c)).

The electron-hole two-body problem in the moiré superlattice can be simplified, taking advantage of the facts that the exciton binding energy (∼100 meV) is much larger than the interlayer hybridization strength ($\sim 10-20$ meV), and that the binding energy variation in the superlattice potential is generally smaller than the bandgap variation. This allows us to treat the exciton problem and the effect of the superlattice in a two-step process. We start by solving the Bethe-Salpeter equations (BSEs) [36, 46] in the absence of the moiré potential and interlayer hybridization,

$$(E_{\tau,c,\mathbf{k}+\mathbf{Q}/2} - E_{\tau,vl,\mathbf{k}-\mathbf{Q}/2})A^\tau_{l\mathbf{Q}}(\mathbf{k}) + \sum_{\mathbf{k}'}\langle \tau l\mathbf{k}\mathbf{Q}|V_{sc}|\tau l\mathbf{k}'\mathbf{Q}'\rangle A^\tau_{l\mathbf{Q}'}(\mathbf{k}') = \mathcal{E}^\tau_l(\mathbf{Q})A^\tau_{l\mathbf{Q}}(\mathbf{k}), \quad (1)$$

where $\mathbf{Q}$ and $\mathbf{k}$ are the center-of-mass and relative momentum of the electron-hole state, $|\tau l\mathbf{k}\mathbf{Q}\rangle \equiv \hat{c}^\dagger_{\tau c\mathbf{k}+\mathbf{Q}/2}\hat{c}_{\tau vl\mathbf{k}-\mathbf{Q}/2}|0\rangle$. $\hat{c}^\dagger(\hat{c})$ is the electron creation (annihilation) operator, and $|0\rangle$ is the ground state at charge neutrality. $E_{\tau c\mathbf{k}} = \hbar^2\mathbf{k}^2/2m^*_c + E_g$ and $E_{\tau vl\mathbf{k}} = -\hbar^2\mathbf{k}^2/2m^*_v + eEld$ are the monolayer conduction (c) and valence (v) band dispersions under the effective mass approximation. $\tau = \pm K$ is the valley index, $l = 1, 2$ concurrently denotes the middle ($l = 1$) and the top ($l = 2$) WSe_2 layers, and E_g is the interlayer bandgap. We adopted the usual convention that $\mathbf{k}$ is measured from the $\pm K$ point of each layer. $\langle \tau l\mathbf{k}\mathbf{Q}|V_{sc}|\tau l\mathbf{k}'\mathbf{Q}\rangle$ represents the direct interlayer Coulomb interaction matrix and V_{sc} is the screened Coulomb interaction obtained by solving the Poisson equation for the trilayer structure (see Supplemental Material for details.) Note that the exchange interaction mentioned above, which couples $+K$ and $-K$ excitons, is absent for the interlayer excitons.

The lowest energy solution of each BSE is the interlayer exciton state X_l with energy $\mathcal{E}^\tau_l(\mathbf{Q})$ and wavefunction,

$$|X_l(\mathbf{Q})\rangle_\tau = \sum_{\mathbf{k}} A^\tau_{l\mathbf{Q}}(\mathbf{k})\hat{c}^\dagger_{\tau c\mathbf{k}+\mathbf{Q}/2}\hat{c}_{\tau vl\mathbf{k}-\mathbf{Q}/2}|0\rangle. \quad (2)$$

We find that the internal wavefunction $A^\tau_{l\mathbf{Q}}(\mathbf{k})$ is nearly independent of $\mathbf{Q}$ and isotropic in $\mathbf{k}$, reminiscent of the $1s$ exciton wavefunction. $\mathcal{E}^\tau_l(\mathbf{Q}) \approx E_{X_l} + \hbar^2\mathbf{Q}^2/M^*_l$ at small $\mathbf{Q}$, where the exciton effective mass M^*_l is renormalized from the bare value $M^0 = m^*_c + m^*_v$ due to the screened interaction. The energy difference $\Delta E^0 \equiv E^0_{X_2} - E^0_{X_1}$ is about 40 meV. We remark that a more accurate account of the exciton problem could be conducted using, for example, the GW-BSE approach combined with *ab initio* bandstructure calculations [46, 48], which, however, falls outside the focus and scope of the this work.

Exciton moiré Hamiltonian.—We now derive a continuum model Hamiltonian for the interlayer excitons, taking into account the effect of the moiré superlattice modulation and interlayer hybridization. For convenience, we will take $\tau = +K$ and suppress the valley index; the

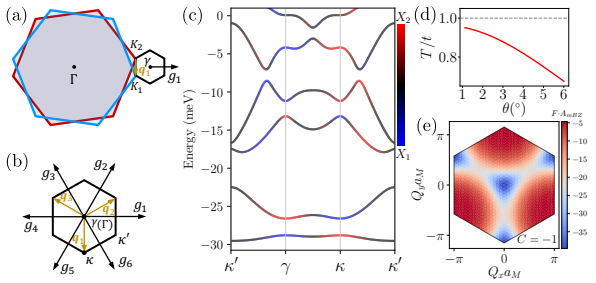

FIG. 2. (a) Rotated Brillouin zones of the middle (cyan) and top (red) WSe_2 layers, and the moiré Brillouin zone (black) of the $tWSe_2$. (b) Exciton moiré Brillouin zone with its center (γ point) set at the origin Γ of momentum space. (c) Bandstructure of hybridized moiré excitons at $\theta = 2.0^\circ$ and $E = \Delta E_0/ed$. Blue (red) line color indicates the fraction of the $X_1(X_2)$ component. (d) The exciton hybridization strength T/t as a function of twist angle. (e) Berry curvature of the lowest exciton band. The corresponding Chern number is $C_0 = 1$.

Hamiltonian at the $-K$ valley can be obtained by time reversal symmetry. Since the valence bands are situated in the $tWSe_2$ superlattice, the hole component of the excitons experience a moiré potential modulation [34]. The moiré potential modulation on the valence bands takes the form [49, 50]

$$U_l(\boldsymbol{r}) = 2V \sum_{i=1,3,5} \cos\big(\boldsymbol{g}_i \cdot \boldsymbol{r} + s_l\phi\big), \tag{3}$$

where V and ϕ are the amplitude and the phase of moiré potential, $s_l = (-1)^{l-1}$. $\boldsymbol{g}_1 = 4\pi/\sqrt{3}a_M(1,0)$ and $\boldsymbol{g}_i = (\hat{\mathcal{R}}_{\pi/3})^{i-1}\boldsymbol{g}_1$ are moiré reciprocal lattice vectors where $\hat{\mathcal{R}}_{\pi/3}$ is counter-clockwise rotation around z axis by $\pi/3$ [Fig. 2(a)]. By Fourier transforming $u_l(\boldsymbol{r})$ and projecting it to the exciton basis in Eq. (2), we obtain the exciton moiré potential,

$$\mathcal{U}_{l,\mathbf{Q},\mathbf{Q}'} = -V\sum_{i=1}^{6} \exp\big(s_{i,l}\phi\big)\delta_{\mathbf{Q}+\boldsymbol{g}_i,\mathbf{Q}'} \tag{4}$$

where $s_{i,l} = (-1)^i s_l$. The minus sign of the amplitude reflects that excitons experience a negative moiré potential compared to the valence electrons (see SM for additional details). The delta function ensures the conservation of exciton COM momentum $\mathbf{Q}$ up to a moire reciprocal vector.

The X_1 and X_2 excitons hybridize with each other via their hole component due to the interlayer hybridization between the valence bands of the twisted WSe_2 bilayers. Because of the presence of the moiré superlattice, the interlayer band hybridization varies periodically in real space with nontrivial layer pseudospin winding [50–52]. In the lowest-order harmonic approximation, it takes the form

$$T(\boldsymbol{r}) = t\sum_n e^{i\boldsymbol{q}_n\cdot\boldsymbol{r}}, \tag{5}$$

where t is the tunneling strength. $\mathbf{q}_1 = \mathbf{K}_2 - \mathbf{K}_1$ is the momentum shift between the K points in the two WSe_2 layers and $\mathbf{q}_n$ is related to $\mathbf{q}_1$ by three-fold rotation $\mathbf{q}_n = (\hat{\mathcal{R}}_{2\pi/3})^{n-1}\mathbf{q}_1$ [Fig. 2(a)]. Note that we ignore the hybridization with the $MoSe_2$ layer because of the large valence band offset between the WSe_2 and $MoSe_2$ layers. Using the same procedure, we obtain the Hamiltonian for hybridization between the X_1 and X_2 excitons,

$$\mathcal{T}_{\mathbf{Q},\mathbf{Q}'} = t\sum_{n=1}^{3}\sum_{\mathbf{k}} A^*_{1,\mathbf{Q}}(\mathbf{k})A_{2,\mathbf{Q}'}\big(\mathbf{k}-\frac{\mathbf{q}_n}{2}\big)\delta_{\mathbf{Q}+\mathbf{q}_n,\mathbf{Q}'}, \tag{6}$$

where the coefficient of the three hoping processes, $T_n \equiv t\sum_{\mathbf{k}} A^*_{1,\mathbf{Q}}(\mathbf{k})A_{2,\mathbf{Q}+\mathbf{q}_n}(\mathbf{k}-\mathbf{q}_n/2)$, depends on the overlap of the exciton internal wavefunctions with a relative shift $\mathbf{q}_n/2$. Because of the C_3 symmetry (around z-axis), the three amplitudes are equal, $T_1 = T_2 = T_3 \equiv T$. $A_{l,\boldsymbol{Q}}(\mathbf{k})$ is real and weakly dependent on $\boldsymbol{Q}$ for small $|\boldsymbol{Q}|$. Figure 2(d) plots T/t as a function of twist angle θ. When θ is small, T/t is close to unity; as θ increases, T/t decreases monotonically mainly due to the $\boldsymbol{q}_n/2$ shift and thus reduced exciton wavefunction overlap. It should be emphasized that the COM momentum of X_2 exciton is measured from $\boldsymbol{\kappa} = \mathbf{K}_2 - \mathbf{K}_1$ instead of $\boldsymbol{\gamma}$ as shown in Fig. 2(b).

Combining Eq. (4) and (6), we arrive at the full exciton moiré Hamiltonian in the basis $\{|X_1\rangle, |X_2\rangle\}$,

$$\mathcal{H}_{\mathbf{Q},\mathbf{Q}'} = \begin{pmatrix} \mathcal{E}_1(\mathbf{Q})\delta_{\mathbf{Q},\mathbf{Q}'} + \mathcal{U}_{1,\mathbf{Q},\mathbf{Q}'} & \mathcal{T}_{\mathbf{Q},\mathbf{Q}'} \\ \mathcal{T}^\dagger_{\mathbf{Q},\mathbf{Q}'} & \mathcal{E}_2(\mathbf{Q})\delta_{\mathbf{Q},\mathbf{Q}'} + \mathcal{U}_{2,\mathbf{Q},\mathbf{Q}'} \end{pmatrix}. \tag{7}$$

The valley projected ($\tau = +K$) Hamiltonian $\mathcal{H}$ respects the C_3, time-reversal $\mathcal{T}$, and $C_{2y}\mathcal{T}$ symmetries, where C_{2y} is two-fold rotation around y-axis. We choose the exciton moiré Brillouin zone (mBZ) whose center (γ point) sits at the origin of COM momentum Γ, as illustrated in Fig. 2(b) and numerically diagonalize $\mathcal{H}$ to obtain the exciton moiré band structure. (See Supplemental Material for more details.)

Exciton topological flatbands.—The exciton moiré bandstructure for a single valley ($\tau = +K$) is shown in Fig. 2(c) at a representative twist angle $\theta = 2.0^\circ$ and under the electric field $E = \Delta E^0/ed$ when E_{X_1} and E_{X_2} cross each other. The bandstructure features two narrow low-energy bands isolated from higher energy bands. A gap opens up between the two as a result of the hybridization between the X_1 and X_2 excitons. The berry curvature of the lowest band, illustrated in Fig. 2(e), exhibit strong amplitudes at high symmetry points γ and κ, reminiscent of a band inversion that occurs at these points. The wavefunctions at these high symmetry points are eigenstates of C_3 transformation, $C_3|\Psi_{n,\boldsymbol{Q}}\rangle = \eta^{C_3}_{n,\boldsymbol{Q}}|\Psi_{n,\boldsymbol{Q}}\rangle$, where n is the band index and the eigenvalues, $\eta^{C_3}_{0,\gamma} = \eta^{C_3}_{0,\kappa} = 1$ for the lowest band ($n = 0$), and $\eta^{C_3}_{1,\gamma} = \eta^{C_3}_{1,\kappa} = e^{i2\pi/3}$ for the sec-

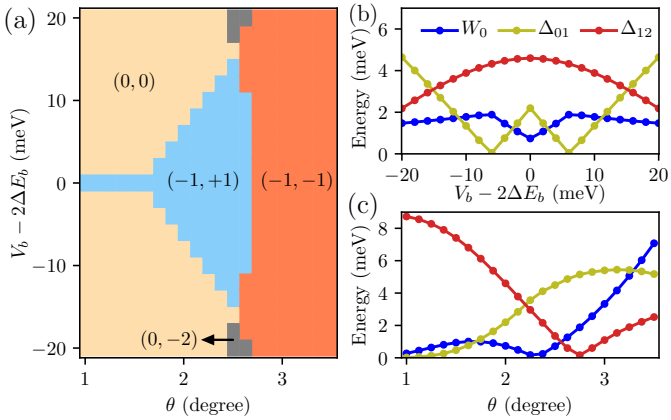

FIG. 3. (a) Topological phase diagram of the moiré exciton bands. The numbers in the parenthesis are (C_0, C_1), the Chern number of the two lowest bands. (b) Bandwidth and energy gap as a function of displacement field at twist angle $\theta = 2.0°$. W_0 is the bandwidth of the lowest ($n = 0$) moiré band. Δ_{01} (Δ_{12}) is the global gap between the $n = 0$ and 1 ($n = 1$ and 2) bands. (c) Bandwidth and energy gap as a function of twist angle at fixed displacement field $V_b = 2\Delta E^0$.

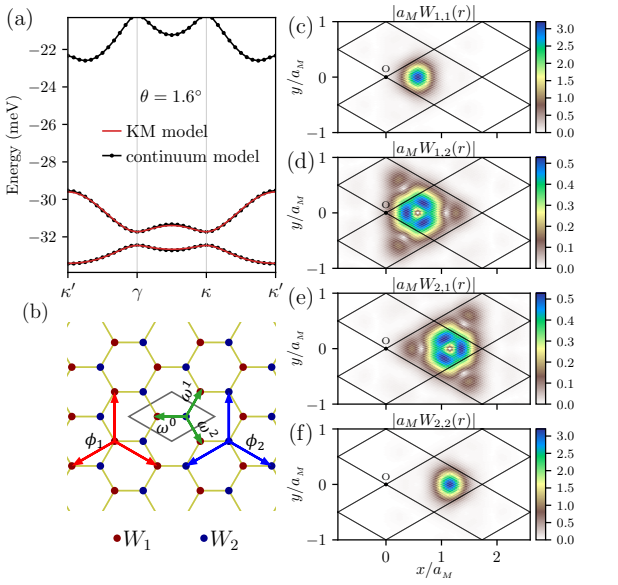

FIG. 4. (a) Bosonic Kane-Mele tight-binding model dispersion (red solid line) in comparison with the band dispersion obtained from the continuum model. (b) Schematic illustration of the Kane-Mele tight-binding model (for valley $\tau = +K$) with nearest (NN) and next-nearest neighbor (NNN) hoppings. ω^n and ϕ_l represent the phase of the NN and NNN hopping processes, where $\omega = e^{i2\pi/3}$ and $l = 1, 2$. The black diamond marks a real space moiré unit cell. (c-f) Amplitudes of the Wannier orbitals in real space. $W_{\alpha,l}$ is the X_l component of the W_α orbital at the moiré site $\boldsymbol{R} = 0$, with $\alpha = 1, 2$. The black grids mark the moiré unit cells.

ond lowest band ($n = 1$), have an inverted order compared to the limit of zero hybridization. ($\eta^{C_3}_{n,\kappa'} = e^{-i2\pi/3}$ for both $n = 0$ and 1.) Note that we factored out the non-moiré angular momentum of excitons (See SM). The Chern numbers of the two lowest bands are $C_0 = -1$ and $C_1 = 1$, indicating that a pair of time reversal symmetry protected bosonic helical edge states exist inside their gap.

Upon varying twist angle and displacement field, the exciton bands display a rich topological phase diagram as illustrated in Fig. 3(a). As the displacement field, measured in energy as $V_b \equiv 2eEd$, is tuned closer to $2\Delta E^0$, the band inversion between the first and second moiré bands occurs, resulting in a topological transition from the trivial phase with $(C_0, C_1) = (0, 0)$ to the topological phase with $(C_0, C_1) = (-1, +1)$. The gap between the two lowest bands Δ_{01} closes at the transition point as shown in Fig. 3(b). For small twist angle $\theta < 1.7°$, the displacement field range for the inverted region is narrow because of the small bandwidths. As θ increases, the $n = 1$ band intersects the higher ($n = 2$) band at around $\theta_c = 2.7°$ (where Δ_{12} vanishes as shown in Fig. 3(c)), leading to a change in the Chern number, from $C_1 = +1$ to $C_1 = -1$ while C_0 remains unchanged. At large $|V_b - 2\Delta E^0|$, this intersection takes place before the topological band inversion between the lowest two bands, yielding a transition from the $(C_0, C_1) = (0, 0)$ phase to the $(C_0, C_1) = (0, -2)$. Interestingly, the bandwidth W_0 of the lowest band exhibits a minimum close to zero at around $\theta_m = 2.3°$, marking the emergence of a "magic angle" for the bosonic topological flatband.

Bosonic Kane-Mele model.—The topology and real space density (see Supplemental Material) of the two lowest moiré bands indicate that they can be described by an effective Kane-Mele lattice model with two orbitals (or sublattices) in each unit cell. To confirm this, we construct Wannier states for the two lowest bands in the regime where the gap to higher energy bands remain open. The Wannier functions are given by

$$|W_\alpha\rangle = \frac{1}{\sqrt{N}} \sum_{n=0,1} \sum_{\boldsymbol{Q}} F^n_{\alpha,\boldsymbol{Q}} |\Psi_{n,\boldsymbol{Q}}\rangle \tag{8}$$

for $\alpha = 1, 2$. $F_{\boldsymbol{Q}}$ is a unitary matrix for fixing the gauge of the wavefunction $|\Psi_{n,\boldsymbol{Q}}\rangle$. We obtain $F_{\boldsymbol{Q}}$ by requiring that $\sum_n F^n_{\alpha,\boldsymbol{Q}} |\Psi_{n,\boldsymbol{Q}}\rangle$ is maximally polarized to its $X_{l=\alpha}$ component and is real at its center (where its amplitude peaks) in real space. (See details in SM and also Ref. [53]). Figure 4(c-f) plot the X_1 and X_2 components of $W_\alpha(\boldsymbol{r}) = [W_{\alpha,1}(\boldsymbol{r}), W_{\alpha,2}(\boldsymbol{r})]^T$ for site $\boldsymbol{R} = 0$. $W_\alpha(\boldsymbol{r})$ has dominant weight in its $W_{\alpha,\alpha}(\boldsymbol{r})$ component and is centered around $\boldsymbol{r} = \boldsymbol{t}_\alpha$, where $\boldsymbol{t}_1 = (1/\sqrt{3}, 0)a_M$ and $\boldsymbol{t}_2 = (2/\sqrt{3}, 0)a_M$ corresponds to the XM and MX positions in the moiré superlattice. We construct the bosonic tight-biding model for the honeycomb lattice formed by the W_1 and W_2 exciton orbitals as shown in Fig. 4(b). The effective lattice Hamiltonian, keeping the nearest

and next-nearest hopping terms, takes the form

$$\mathcal{H}_{eff}^{+K} = -\sum_{\alpha,i}\sum_{m=1}^{3} t^{(2)} e^{i\phi_\alpha} \hat{b}^\dagger_{\alpha,\boldsymbol{R}_i+\boldsymbol{a}_m} \hat{b}_{\alpha,\boldsymbol{R}_i} - \sum_{\alpha,i}\sum_{m=1}^{3} t^{(1)} e^{i\omega^{m-1}} \hat{b}^\dagger_{1,\boldsymbol{R}_i+\boldsymbol{\delta}_m} \hat{b}_{2,\boldsymbol{R}_i} + h.c. \quad (9)$$

where $\hat{b}^\dagger_{\alpha,\boldsymbol{R}_i}$ is the creation operator for the $W_{\alpha,\boldsymbol{R}_i}$ state. $\boldsymbol{a}_1 = (\sqrt{3}/2, -1/2)a_M$ and $\boldsymbol{a}_m = (\hat{\mathcal{R}}_{\pi/3})^{m-1}\boldsymbol{a}_1$ are real lattice vectors, and $\boldsymbol{\delta}_m = \{\boldsymbol{0}, -\boldsymbol{a}_3, \boldsymbol{a}_1\}$. The first term is the intra-sublattice hopping with amplitude $t^{(2)}$ and phase ϕ_α. $\phi_1 = 0$ and $\phi_2 = \boldsymbol{\kappa}\cdot\boldsymbol{a}_1$ in the limit of zero hybridization, $T = 0$, and gradually deviates from these values as T is increased. The second term is the nearest inter-orbital hopping term where $\omega = e^{i2\pi/3}$. The bond dependent phase seemingly breaks C_3 symmetry but in fact does not. This is because $|W_1\rangle$ and $|W_2\rangle$ transform differently under C_3, $C_3|W_{1,\boldsymbol{R}}\rangle = |W_{1,\boldsymbol{R}'}\rangle$ and $C_3|W_{2,\boldsymbol{R}}\rangle = \omega|W_{2,\boldsymbol{R}'}\rangle$ with $\boldsymbol{R}' + \boldsymbol{t}_\alpha = \hat{\mathcal{R}}_{\pi/3}(\boldsymbol{R} + \boldsymbol{t}_\alpha)$ (See SM for details). $\mathcal{H}_{eff}^{+K}$ is thus a modified version of the Haldane Hamiltonian [55] (and can mapped to the original version by a simple momentum shift, $\mathcal{H}_{eff}^{+K}(\boldsymbol{Q}) = \mathcal{H}_{Haldane}(\boldsymbol{Q} - \boldsymbol{\kappa}')$). The two valley copies of the effective Hamiltonian, $\mathcal{H}_{eff}^{\pm K}$, together form the Kane-Mele (KM) model [56]. The dispersion of the effective KM model agrees well with the continuum model bandstructure as illustrated in Fig. 4(a), confirming the accuracy of truncating at the NNN hoppings.

Discussions and Outlook.—The tWX_2/MoX_2 moiré heterostructure we propose realizes topological excitons with extended lifetimes, crucial for exploring strongly correlated many-body exciton phases, and establishes a new mechanism for inducing exciton topology that has not been explored before. Most excitingly, it provides a promising route for realizing the first solid-state-based platform for the bosonic Kane-Mele model, which features topological flatbands and is therefore capable of simulating strongly correlated topological bosons with unprecedented controllability.

It has been predicted that in a Kane-Mele model with flatbands interacting hardcore bosons , the ground state is an abelian FQAHE state at $\nu = 1/2$ [57] and exhibit non-abelian quantum Hall effect (NA-QHE) at $\nu = 1$ [58], both in the absence of Landau levels. The interlayer moiré excitons can be generated by optical excitations and a finite quasi-equilibrium population can be sustained thanks to the slow exciton recombination rate. Given the success in the observation of a bosonic Mott insulator, we are optimistic that the proposed structure can support a rich set of topological versions of the strongly correlated insulator, including the FQAHE and NA-QHE insulators.

The hallmark of nontrivial exciton topology is the helical edges states inside the topological gap which can potentially be probed by optical reflection measurement [59] with polarization sensitivity and spatial resolution down to the moiré scale. A recent experiment [60] demonstrated visualization of real space exciton wavefunction using local scanning probe coupled with optical current which can also be used for imaging the bosonic helical edge states. On the other hand, the circular polarization information of emitted excitons can reveal the berry curvature of bulk exciton moiré bands [61].

Acknowledgment.—The authors acknowledge helpful discussions with Allan MacDonald, You Zhou, Jiabin Yu, Beini Gao, and Lifu Zhang. This work was supported by Laboratory for Physical Sciences.

* mingxie@umd.edu

[1] Y. Tang, L. Li, T. Li, Y. Xu, S. Liu, K. Barmak, K. Watanabe, T. Taniguchi , A. H. MacDonald , J. Shan, and K. F. Mak, Nature **579**, 353 (2020).
[2] E. C. Regan, D. Wang, C. Jin, M. I. B. Utama, B. Gao, X. Wei, S. Zhao, W. Zhao, Z. Zhang, K. Yumigeta, M. Blei, J. D. Carlström, K. Watanabe, T. Taniguchi, S. Tongay, M. Crommie, A. Zettl, and F. Wang, Nature **579**, 359 (2020).
[3] Y. Xu, S. Liu, D. A. Rhodes, K. Watanabe, T. Taniguchi, J. Hone, V. Elser, K. F. Mak, and J. Shan, Nature **587**, 214 (2020).
[4] L. Wang, E.-M. Shih, A. Ghiotto, L. Xian, D. A. Rhodes, C. Tan, M. Claassen, D. M. Kennes, Y. Bai, B. Kim, K. Watanabe, T. Taniguchi, X. Zhu, J. Hone, A. Rubio, A. N. Pasupathy, and C. R. Dean, Nat. Mater. **19**, 861 (2020).
[5] Z. Zhang, Y. Wang, K. Watanabe, T. Taniguchi, K. Ueno, E. Tutuc, and B. J. LeRoy, Nat. Phys. **16**, 1093 (2020).
[6] C. Jin, Z. Tao, T. Li, Y.Xu, Y. Tang, J. Zhu, S. Liu, K. Watanabe, T. Taniguchi, J. C. Hone, L. Fu, J.Shan, and K. F. Mak, Nat. Mater. **20**, 940 (2021).
[7] T. Li, S.Jiang, L. Li, Y. Zhang, K. Kang, J. Zhu, K. Watanabe, T. Taniguchi, D. Chowdhury, L. Fu, J. Shan, and K. F. Mak, Nature **597**, 350 (2021).
[8] S. Shabani, D. Halbertal, W. Wu, M. Chen, S. Liu, J. Hone, W. Yao, D. N. Basov, X. Zhu, and A. N. Pasupathy, Nat. Phys. **17**, 720 (2021).
[9] X. Huang, T. Wang, S. Miao, C. Wang, Z. Li, Z. Lian, T. Taniguchi, K. Watanabe, S. Okamoto, D. Xiao, S.-F. Shi, and Y.-T. Cui, Nat. Phys. **17**, 715 (2021).
[10] Y. Tang, J. Gu, S. Liu, K. Watanabe, T. Taniguchi, J. C. Hone, K. F. Mak, J. Shan, Nat. Comm. **13**, 4271 (2022).
[11] A. Ghiotto, E.-M. Shih, G. S. S. G. Pereira, D. A. Rhodes, B. Kim, J. Zang, A. J. Millis, K. Watanabe, T. Taniguchi, J. C. Hone, L. Wang, C. R. Dean, and A. N. Pasupathy, Nature **597**, 345 (2021).
[12] W. Zhao, B. Shen, Z. Tao, Z. Han, K. Kang, K. Watanabe, T. Taniguchi, K. F. Mak, and J. Shan, Nature **616**, 61 (2023).
[13] T. Li, S. Jiang, B. Shen, Y. Zhang, L. Li, T. Devakul, K. Watanabe, T. Taniguchi, L. Fu, J. Shan, and K. F. Mak, Nature **600**, 641 (2021).
[14] J. Cai, E. Anderson, C. Wang, X. Zhang, X. Liu, W.

Holtzmann, Y. Zhang, F. Fan, T. Taniguchi, K. Watanabe, Y. Ran, T. Cao, L. Fu, D. Xiao, W. Yao, and X. Xu, Nature (London) **622**, 63 (2023).
[15] Y. Zeng, Z. Xia, K. Kang, J. Zhu, P. Knüppel, C. Vaswani, K. Watanabe, T. Taniguchi, K. Fai Mak, and J. Shan, Nature (London) **622**, 69 (2023)
[16] H. Park, J. Cai, E. Anderson, Y. Zhang, J. Zhu, X. Liu, C. Wang, W. Holtzmann, C. Hu, Z. Liu, T. Taniguchi, K. Watanabe, J.-H. Chu, T. Cao, L. Fu, W. Yao, C.-Z. Chang, D. Cobden, D. Xiao, and X. Xu, Nature (London) **622**, 74 (2023).
[17] F. Xu, Z. Sun, T. Jia, C. Liu, C. Xu, C. Li, Y. Gu, K. Watanabe, T. Taniguchi, B. Tong, J. Jia, Z. Shi, S. Jiang, Y. Zhang, X. Liu, and T. Li, Phys. Rev. X **13**, 031037 (2023).
[18] B. A. Foutty, C. R. Kometter, T. Devakul, A. P. Reddy, K. Watanabe, T. Taniguchi, L. Fu, and B. E. Feldman, arXiv:2304.09808.
[19] Z. Tao, B. Shen, S. Jiang, T. Li, L. Li, L. Ma, W. Zhao, J. Hu, K. Pistunova, K. Watanabe, T. Taniguchi, T. F. Heinz, K. Fai Mak, and J. Shan, Phys. Rev. X **14**, 011004 (2024).
[20] K. Kang, B. Shen, Y. Qiu, K. Watanabe, T. Taniguchi, J. Shan, and K. F. Mak, arXiv:2402.03294.
[21] K. Kang, Y. Qiu, K. Watanabe, T. Taniguchi, J. Shan, and K. F. Mak, arXiv:2402.04196.
[22] E. Tang, J.-W. Mei, and X.-G. Wen, Phys. Rev. Lett. **106**, 236802 (2011).
[23] K. Sun, Z. Gu, H. Katsura, and S. Das Sarm, Phys. Rev. Lett. 106, 236803 (2011).
[24] T. Neupert, L. Santos, C. Chamon, and C. Mudry, Phys. Rev. Lett. **106**, 236804 (2011).
[25] N. Regnault and B. A. Bernevig, Phys. Rev. X **1**, 021014 (2011).
[26] D. N. Sheng, Z.-C. Gu, K. Sun, and L. Sheng, Nat. Comm. **2**, 389 (2011).
[27] K. L. Seyler, P. Rivera, H. Yu, N. P. Wilson, E. L. Ray, D. G. Mandrus, J. Yan, W. Yao, X. Xu, Nature **567**, 66 (2019).
[28] K. Tran, G. Moody, F. Wu, X. Lu, J. Choi, K. Kim, A. Rai, D. A. Sanchez, J. Quan, A. Singh, J. Embley, A. Zepeda, M. Campbell, T. Autry, T. Taniguchi, K. Watanabe, N. Lu, S. K. Banerjee, K. L. Silverman, S. Kim, E. Tutuc, L. Yang, A. H. MacDonald, and X. Li, Nature **567**, 71 (2019).
[29] C. Jin, E. C. Regan, A. Yan, M. Iqbal Bakti Utama, D. Wang, S. Zhao, Y. Qin, S. Yang, Z. Zheng, S. Shi, K. Watanabe, T. Taniguchi, S. Tongay, A. Zettl, and F. Wang, Nature **567**, 76 (2019).
[30] E. M. Alexeev, D. A. Ruiz-Tijerina, M. Danovich, M. J. Hamer, D. J. Terry, P. K. Nayak, S. Ahn, S. Pak, J. Lee, J. I. Sohn, M. R. Molas, M. Koperski, K. Watanabe, T. Taniguchi, K. S. Novoselov, R. V. Gorbachev, H. S. Shin, V. I. Fal'ko, and A. I. Tartakovskii, Nature **567**, 81 (2019).
[31] E. Liu, E. Barré, J. van Baren, M. Wilson, T. Taniguchi, K. Watanabe, Y. T. Cui, N. M. Gabor, T. F. Heinz, Y. C. Chang, C. H. Lui, Nature **594**, 46 (2021).
[32] Z. Zhang, E. C. Regan, D. Wang, W. Zhao, S. Wang, M. Sayyad, K. Yumigeta, K. Watanabe, T. Taniguchi, S. Tongay, M. Crommie, A. Zettl, M. P. Zaletel, F. Wang, Nat. Phys. **18**, 1214–1220 (2022).
[33] L. Zhang, F. Wu, S. Hou, Z. Zhang, Y. H. Chou, K. Watanabe, T. Taniguchi, S. R. Forrest, H. Deng, Nature **591**, 61–65 (2021).
[34] F. Wu, T. Lovorn, A. H. MacDonald, Phys. Rev. Lett. **118**, 147401 (2017).
[35] H. Yu, G.-B. Liu, J. Tang, X. Xu, W. Yao, Sci. Adv. **3**, e1701696 (2017).
[36] F. Wu, T. Lovorn, and A. H. MacDonald, Phys. Rev. B **97**, 035306 (2018).
[37] H. Yu, Y. Wang, Q. Tong, X. Xu, and W. Yao, Phys. Rev. Lett. 115, 187002 (2015).
[38] H. Yu and W. Yao Phys. Rev. X 11, 021042 (2021).
[39] R. Xiong, J. H. Nie, S. L. Brantly, P. Hays, R. Sailus, K. Watanabe, T. Taniguchi, S. Tongay, and C. Jin, Science **380**,860 (2023).
[40] H. Park, J. Zhu, X. Wang, Y. Wang, W. Holtzmann, T. Taniguchi, K. Watanabe, J. Yan, L. Fu, T. Cao, D. Xiao, D. R. Gamelin, H. Yu, W. Yao, and X. Xu, Nat. Phys. **19**, 1286 (2023).
[41] B. Gao, D. G. Suárez-Forero, S. Sarkar, T.-S. Huang, D. Session, M. J. Mehrabad, R. Ni, M. Xie, J. Vannucci, S. Mittal, K. Watanabe, T. Taniguchi, A. Imamoglu, Y. Zhou, and M. Hafezi, arXiv:2304.09731
[42] S. Miao, T. Wang, X. Huang, D. Chen, Z. Lian, C. Wang, M. Blei, T. Taniguchi, K. Watanabe, S. Tongay, Z. Wang, D. Xiao, Y.-T. Cui, and S.-F. Shi, Nat. Comm. **12**, 3608 (2021).
[43] The TMD species must be chosen to met the following conditions: (1) the MX_2 and $M'X_2$ have a type-II band alignment; (2) the interlayer gap is direct such that the X_1 and X_2 excitons are the lowest energy excitons. Twisted WSe_2 and $MoTe_2$ homobilayers are the only experimental verified examples which have a nontrivial topological interlayer hybridization . We chose the WSe_2 since the common chalcogen TMD of $MoTe_2$, i.e., WTe_2, does not have a stable R-Type crystal structure.
[44] F. Wu, F. Qu, and A. H. MacDonald, Phys. Rev. B **91**, 075310 (2015).
[45] H. Yu, G.-B. Liu, P. Gong, X. Xu, and Wang Yao, Nat. Comm. **5**, 3876 (2014).
[46] D. Y. Qiu, T. Cao, and S. G. Louie Phys. Rev. Lett. **115**, 176801 (2015).
[47] T. Cao, G. Wang, W. Han, H. Ye, C. Zhu, J. Shi, Q. Niu, P. Tan, E. Wang, B. Liu, and J. Feng, Nat. Comm. **3**, 887 (2012).
[48] M. Rohlfing and S. G. Louie, Phys. Rev. B **62**, 4927 (2000).
[49] F. Wu, T. Lovorn, E. Tutuc, and A. H. MacDonald, Phys. Rev. Lett. **121**, 026402 (2018)
[50] F. Wu, T. Lovorn, E. Tutuc, I. Martin, and A. H. MacDonald, Phys. Rev. Lett. **122**, 086402 (2019).
[51] H. Pan, F. Wu, and S. Das Sarma, Phys. Rev. Research **2**, 033087 (2020)
[52] T. Devakul, V. Crépel, Y. Zhang, and L. Fu, Nat. Comm. **12**, 6730 (2021).
[53] X.-J. Luo, M. Wang, and F. Wu, Phys. Rev. B 107, 235127 (2023).
[54] C. Fang, M. J. Gilbert, and B. A. Bernevig, Phys. Rev. B **86**, 115112 (2012).
[55] F. D. M. Haldane, Phys. Rev. Lett. **61**, 2015 (1988).
[56] C. L. Kane and E. J. Mele, Phys. Rev. Lett. **95**, 226801 (2005).
[57] Y.-F. Wang, Z.-C. Gu, C.-D. Gong, and D. N. Sheng, Phys. Rev. Lett. **107**, 146803 (2011).
[58] Y.-F. Wang, H. Yao, Z.-C. Gu, C.-D. Gong, and D. N. Sheng, Phys. Rev. Lett. **108**, 126805 (2012).

[59] E. Barré, O. Karni, E. Liu, A. L O'Beirne, X. Chen, H. B Ribeiro, L. Yu, B. Kim, K. Watanabe, T. Taniguchi, K. Barmak, C. H. Lui, S. Refaely-Abramson, F. H da Jornada, and F. F Heinz, Science **376**, 406 (2022).

[60] H. Li, Z. Xiang, M. H. Naik, W. Kim, Z. Li, R. Sailus, R. Banerjee, T. Taniguchi, K. Watanabe, S. Tongay, A. Zettl, F. H. da Jornada, S. G. Louie, M. F. Crommie, and F. Wang, Nat. Mater. (2024).

[61] M. Schüler, U. De Giovannini, H. Hübener, A. Rubio, M. A. Sentef, P. Werner, Sci. Adv. **6**, eaay2730 (2020).